Effective algorithm for simulations of layer-by-layer growth during pulsed-laser deposition

Vít Gabriel* and Pavel Kocán
Department of Surface and Plasma Science, Faculty of Mathematics and Physics, Charles University, V Holešovičkách 2, 180 00 Prague 8, Czech Republic

Václav Holý
Department of Condensed Matter Physics, Faculty of Mathematics and Physics, Charles University, Ke Karlovu 5, 121 16 Prague 2, Czech Republic

(Received 15 July 2020; revised 12 October 2020; accepted 24 November 2020; published 14 December 2020)

The atomistic simulation of materials growing in the layer-by-layer mode by the pulsed-laser deposition is a significant challenge mainly due to the short timescales in which the fastest processes on the surface occur together with long periods between pulses. We present a kinetic Monte Carlo algorithm which overcomes the scaling problem by approximation of fast diffusion and by neglecting complex chemical processes. The atomic diffusion is modeled as a two-dimensional gas of material units on each layer. The model is based on a few elementary processes—the condensation of units on the surface, their dissolution back to the gas, and interlayer transport, which can be influenced by the Ehrlich-Schwoebel barrier. With these simplifications, the computational time of the algorithm scales only linearly with the size of the substrate while describing physically relevant growth kinetics. We demonstrate that the simplified model is suitable for simulations of layered growth of thin films in the range from quasicontinuous deposition to low-frequency cases. The model is successfully implemented to provide an alternative explanation of the time evolution of layer coverages by interlayer transport after pulses of deposition experimentally observed during perovskite growth [G. Eres *et al.*, Phys. Rev. B **84**, 195467 (2011)].

DOI: 10.1103/PhysRevE.102.063305

I. INTRODUCTION

The ability to control the epitaxial growth of thin films is of great importance with respect to the synthesis of films with desired properties. This is currently true, for example, in the case of the pulsed-laser deposition (PLD) growth of perovskites group materials [1–3].

From real-time experiments, it is usually possible to obtain spatially integrated information related to the growth kinetics, typically the coverage of the growing layers. However, the underlying kinetics is difficult to extract. For this reason, computer simulations are an important technique that is complementary to the experiments since it allows one to test the proposed kinetics by calculating the evolution of atomically resolved morphologies, from which the experimentally relevant quantities can be obtained.

Different modes of thin film growth appear depending on the binding energies to the substrate and neighboring atoms or molecules. In the so-called layer-by-layer (LBL) mode, the deposited material forms partially covered two-dimensional (2D) planes on the surface. We use the less strict definition of the LBL growth, in which several uncovered layers coexist. Note that the true LBL growth in which a new layer starts growing once the previous one is completed is not possible [4]. The LBL mode is often desired because it results in the growth of well-defined homogeneous films. An example of materials which grow in the LBL mode is the so-called layered perovskites. These materials have the same general formula ABO_3, where A and B are metal cations and O is oxygen. Depending on the combination of the metals A and B, the materials can demonstrate a large variety of interesting phenomena, for example, superconductivity [5], ferroelectricity [6], or ferromagneticity [7].

The properties of the resulting films are also significantly influenced by the deposition regime. Typical examples of methods with continuous deposition are molecular beam epitaxy and vacuum sputtering, while the most prominent pulsed methods are the pulsed-plasma deposition and the PLD. In the PLD mode, a target is heated by a high-power laser which, during very short times, evaporates a small amount of atoms or molecules (units). Due to the high power of the laser and thus the high temperature of the target, the impinging units on the substrate are significantly hotter than the substrate. Hence, the system is not in a thermodynamic equilibrium. Under correct conditions, the PLD growth allows one to obtain smoother surfaces than the continuous deposition [8]. Moreover, the PLD has an advantage of the possibility to tune the surface smoothness by the laser repetition frequency [9,10].

The PLD growth kinetics has been investigated *in situ* by several x-ray scattering methods; however, the analysis of the experimental data requires a suitable model. Several models of PLD growth have been published so far. In the rate-equation approach, the time development of the distribution of the

*vit.gabriel@mff.cuni.cz

monolayer islands during the deposition is described by a set of differential equations, which can be easily solved [11–13]. A simpler way is based on the calculation of the time evolution of the monolayer coverages [14]. These models, however, cannot be used for the simulation of *in situ* x-ray scattering since they do not describe the time evolution of island shapes. The level-set method [15,16] presents a phenomenological model for the simulation of the time development of the morphology of a growing surface.

Another possible approach is to use a (kinetic) Monte Carlo (kMC) algorithm based on the random generation of a sequence of atomistic processes selected in each step with respect to their probabilities. The film morphology is simulated by kMC in a nonintegrated way, but with consequences on the computational costs of the algorithm, in which the diffusion of the units significantly slows the simulations. This issue is even more substantial in the case of PLD simulations with fast diffusion of energetic atoms or molecules. Using this technique, without model simplifications, it is usually possible to simulate only submonolayer growth [17] or few-monolayer growth on small substrates ranging from 50×50 to 100×100 adsorption sites [18,19], which is less than the coherence length of x-ray sources and thus insufficient for simulations of *in situ* x-ray scattering. A more realistic approach in which the model simulates the whole deposition, including the interaction of impinging atoms with inert gas, has been applied on the growth of metal films [20]. In the case of diatomic molecules, the model has been expanded to include the chemical processes necessary to create the molecules [21]. However, these techniques are not suitable for simulations of complex materials such as perovskites due to their complicated structure and number of possible chemical reactions influencing the growth.

Here we present a modification of the kMC simulation of the LBL growth by PLD, which overcomes this limitation and substantially speeds up the simulation. As the main approximation, we use a 2D gas of noncondensed material instead of a random walk of each unit. It allows us to compute the growth on several micrometers large substrates over tens of minutes of deposition time. The simulated domain size is higher than the coherence length of the x-ray sources used in techniques sensitive to the morphology of the growing layer, such as grazing-incidence small-angle x-ray scattering, which, in principle, allows interpretation of these experiments on a microscopical level. Here the model is successfully applied to simulate the experimentally obtained interlayer transports of $SrTiO_3$ (STO) [14], providing an alternative explanation of the underlying kinetics.

II. DESCRIPTION OF THE MODEL

The model introduced here was designed to simulate large spatial and timescales of growth at affordable computational costs. Diffusion of atoms or molecules consumes most of the computer time of any kMC-based model used to study the growth of thin films. This leads to compromises in the simulation domain size or simulated time. Our model was created in order to simulate LBL growth of domains that are several micrometers large during tens of minutes without the need to use unrealistically high deposition rates. The diffusion of atoms or molecules is not calculated realistically, instead, the diffusing species are replaced—in the fast diffusion limit—by a 2D gas entity with density ρ_i on the ith layer. This implies that site-specific diffusion along the edges or corners of growing steps is not included in the model.

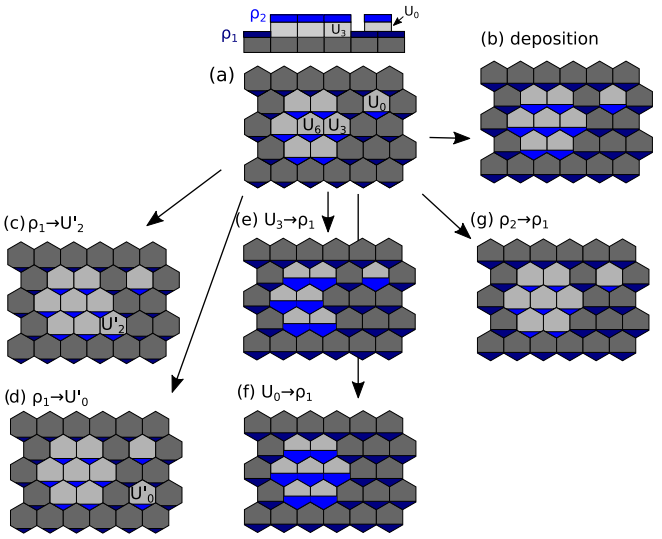

FIG. 1. Illustration of possible processes implemented in the model. (a) Side and top view of the initial state, (b) deposition, (c),(d) condensation, (e),(f) dissolution, and (g) interlayer transport. ρ_i is the 2D gas density on the ith level, represented by an area of the filled part of hexagons. U_N is a condensed unit with N neighbors.

The model is coarse grained, with the smallest condensed unit representing the periodically repeating cell of the growing crystal. Note that the condensed unit may substitute several chemically different atoms in the real growing layer. The chemical interactions necessary for the units to form are not considered, in order to keep the model as simple as possible. Thus the deposited material can be found in two entities: either as the condensed units on which further growth may occur (gray color in Fig. 1) or as the 2D gas of free unbound units (blue color in Fig. 1). The surface geometry is fixed and the growth can occur only on top of the existing condensed units. The 2D gas densities ρ_i are given by the discrete number of the unbound units N_i on the layer i and by the exposed condensed surface, θ_i, $\rho_i = N_i u/\theta_i$, where u is the amount of material corresponding to one condensed unit.

There are four different processes which can occur during any given time step, as shown in Fig. 1: deposition, condensation, dissolution, and interlayer transport. The latter two processes are thermally activated.

The deposition [Fig. 1(b)] occurs in time intervals defined by the laser repetition frequency. In each deposition step, there are multiple units added to the 2D gas based on the average deposition rate. For each arriving unit, the target layer i is chosen with a probability that is proportional to its exposed surface θ_i. Consequently, ρ_i is increased by u/θ_i.

The process of condensation is illustrated in Figs. 1(c) and 1(d). One unit is removed from the 2D gas on the given layer and a new condensed unit is formed at a randomly chosen position of the layer. It is assumed that the condensation is a zero-barrier process and the probability of condensation

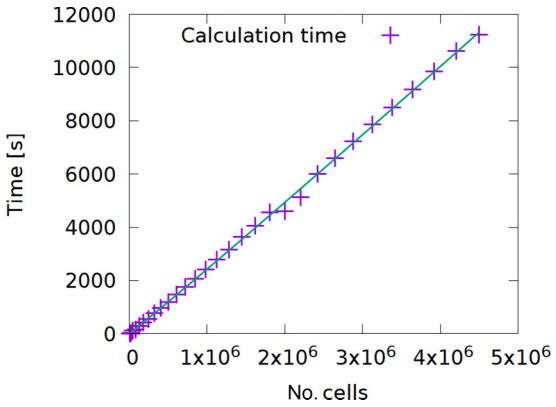

FIG. 2. The dependence of computational time on the number of cells.

at each uncovered position is given by $\rho_i \nu_0$, where ν_0 is the frequency prefactor. Note that the unit condensation is not sensitive to the configuration of the surrounding cells, e.g., the processes in Figs. 1(c) and 1(d) have the same probabilities.

Dissolution [Figs. 1(e) and 1(f)] is the process opposite to the condensation. During this event, a selected cell is removed and the number of units in the 2D gas at the level is increased by one. The activation energy of this process is given by the binding energy to neighbors E_n and to the substrate E_s,

$$\Delta E = E_s + iE_n, \tag{1}$$

where i is the number of neighboring condensed cells on the same level. The more neighbors each cell has, the higher is the activation energy and thus the lower is the probability of dissolution.

The interlayer transport [Fig. 1(g)] is simulated by the process, in which one unit is transferred from the 2D gas of the selected level to the 2D gas of the level that is one tier lower. The rate of this process is proportional to the number of step-edge positions of the layer and to the corresponding 2D gas density. The activation barrier is the parameter corresponding to the Ehrlich-Schwoebel (ES) barrier, E_{ES} [22,23].

For simulations, we used the rejection-free Bortz-Kalos-Lebowitz kinetic Monte Carlo algorithm [24]. The substrate temperature was set to 900 K and the prefactor was set to $\nu_0 = 10^{11}$ s^{-1}. All data presented in Secs. III and IV were calculated using the substrate of 5000 × 2500 cells with hexagonal geometry.

In order to determine the simulation-time efficiency of the algorithm, we plot in Fig. 2 the runtime dependence on the number of cells of the simulated area. The data were fitted by the curve $f(x) = ax^b + c$, with the parameter b obtained from the fit equal to 1.026, which is very close to the ideal linear scaling with the grid size. The scaling with the number of cells, N, in the case of standard models with realistic adatom diffusion is typically N^2, or $N^{3/2}$ if the event choice procedure is optimized [25]. The difference is due to a faster reaching of a stable position by random trial than by the random walk. For testing purposes, we compared the presented model with a model with realistic adatom diffusion. The number of events necessary to simulate the same period of growth increased ∼1000 times on the sample with 5000 units.

III. INFLUENCE OF DEPOSITION REPETITION FREQUENCY

As the output of the results obtained from the kMC simulations, we use morphologies of grown layers together with the calculated quantity I_X corresponding to the time-resolved surface x-ray diffraction (SXRD) measurements [26,27]. For the SXRD measurements performed at the anti-Bragg position, the scattering intensity reduces to a form involving the difference in coverages for even and odd layers [28],

$$I_X = \sum_{n=0}^{\infty} (-1)^n (\theta_n - \theta_{n+1}), \tag{2}$$

where θ_n is the coverage of layer n. This equation is a basic result in SXRD to study growth kinetics using x-ray diffraction.

At first, we confirmed the physically correct behavior of the model on a testing set of simulations with varied binding energies and ES barrier. The details are given in the Appendix A. The parameters of the PLD layers can be tuned by the laser repetition frequency. In the following, we study the influence of the repetition frequency on film morphology using the presented model. Figure 3 shows the results for three repetition frequencies, 5, 0.5, and 0.05 Hz. In all of the cases, the mean deposition rate was 0.0135 ML/s. The neighbor and surface binding energies were 0.5 eV, while the ES barrier was set to zero. The snapshots of morphologies were taken right before a new deposition flux, i.e., in the most stabilized states during the growth. The presented morphologies are recorded after the same period of time since the beginning of growth, long enough to eliminate an influence of the initial substrate state (which can vary in experiment) on the morphology.

The results, simulated in a quasicontinuous mode with repetition frequency 5 Hz, are shown in Fig. 3(a). The snapshot of morphology shows that the simulation is producing small compact faceted islands randomly connected by a coalescence. Coverages of successive layers [right panel of Fig. 3(a)] show that for this combination of parameters, the growth is close to exactly layer by layer: a new layer starts growing when the previous one is almost fully occupied. The same observation can be made from the SXRD which shows periodical peaks reaching the peak value close to unity. A true LBL growth mode would be obtained if the binding energies were set close to zero. However, the instability of condensed units would result in the simulation time approaching infinity.

The results for the repetition frequency 0.5 Hz are shown in Fig. 3(b). As evident from the morphology snapshot, the decrease of the repetition frequency results in a much smaller size of the islands, while their shape is not affected. The size difference is caused by the pronounced nucleation after each pulse due to the higher amount of material deposited per pulse. The time evolution of the level coverages and SXRD are not strongly affected by the decreased repetition rate, except for the appearance of small steps.

Figure 3(c) was obtained with repetition frequency 0.05 Hz, which corresponds to ∼3.7 pulses per deposited layer. The islands can no longer be considered compact or close to circular, and the morphology is rather semicontinuous. This is again caused by the high amounts of material

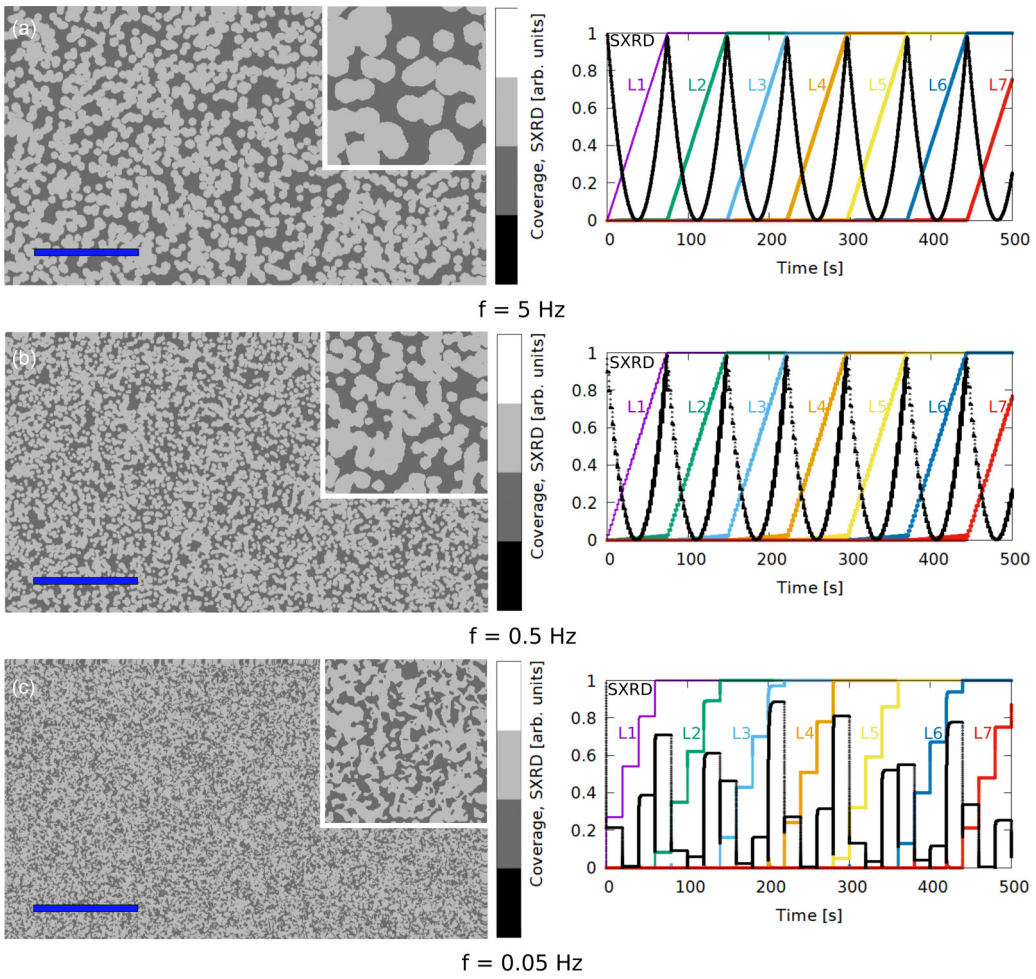

FIG. 3. Morphologies and SXRDs for various repetition frequencies: the L1–L9 labels denote the layer, the blue line is 0.5 μm long, and the size of one molecule is considered to be 0.533 nm. The size of the insets is 500 × 500 units, i.e., 266.5 × 266.5 nm.

deposited per pulse and the resultant pronounced nucleation. The system quickly gets to a stable state after each pulse, as evident from the steplike shape of evolution of the level coverages. Another visible effect is the appearance of small peaks at the coverages of one level higher than the currently active one, for example, "Level 4" at 200 seconds. These peaks quickly disappear due to the interlayer transport mediated by the zero ES barrier. The same effect can be seen on the shape of the SXRD as well. Immediately after each pulse, the value of the SXRD drops because of deposition on top of the active layer, and the value of the SXRD starts growing again due to filling of the active layer by the interlayer transport.

IV. APPLICATION OF THE MODEL ON GROWTH OF STO

Next, we discuss application of the model to the data obtained by experimental studies of interlayer transport during STO growth by PLD. In Ref. [14], the authors used SXRD to monitor the evolution of coverage on active layers after deposition pulses. The observed interlayer transport has been fitted by a biexponential function [14], which was interpreted by the coexistence of fast and slow mechanisms of the transport. The timescales of the fast and slow transport are few milliseconds and several seconds, respectively. Using our model, we were able to reproduce the SXRD data from Ref. [14] by calculating proper energy barriers without the need of any further model modifications.

We assumed that the observed biexponential behavior, and hence slow and fast interlayer transport, are caused by dissolution of units with zero and one neighbor, respectively, with a subsequent jump down to the lower level. Because only the dissolved units can get to the lower level, the rate of the observed interlayer transport is expected to be proportional to the dissolution rate.

The time constants τ_1 and τ_2 of both interlayer transports have been calculated in Ref. [14] from the time change of the level coverages. Binding energies E_s and E_n can be obtained by solving two equations:

$$\tau_1^{-1} = \nu_0 \exp\left(-\frac{E_s}{k_b T}\right), \tag{3}$$

$$\tau_2^{-1} = \nu_0 \exp\left(-\frac{E_s + E_n}{k_b T}\right). \tag{4}$$

The values corresponding to $\tau_1 = 0.9$ and $\tau_2 = 12.4$ s with parameter $T = 940$ K are $E_s = 2.05$ and $E_n = 0.2$ eV.

In Fig. 4, we present the simulated SXRD intensity and the level coverages. The time period between pulses was 50 s and during one pulse 0.083 monolayers were deposited. Both

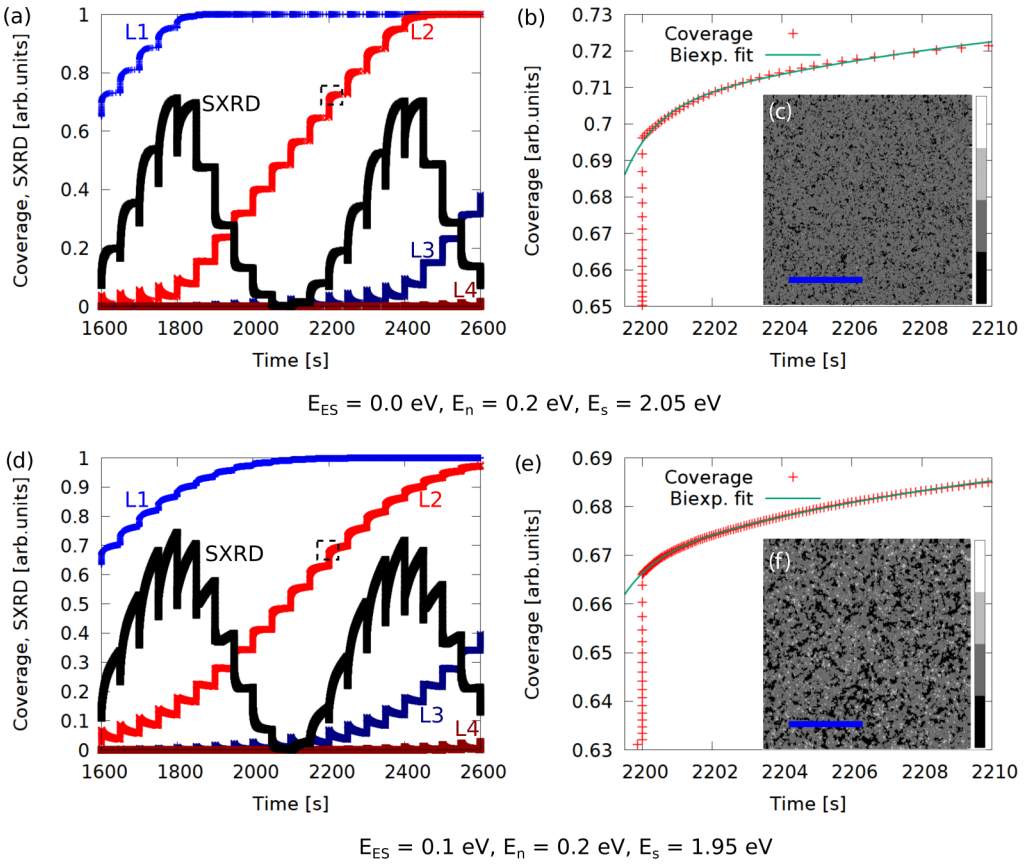

FIG. 4. (a),(d) The SXRD of part of the deposition and (b),(e) a detail on one transient with the biexponential fit proposed in [14]. (c),(f) The sample of the morphology; the blue line is 100 nm long. The rectangle in (a) and (d) marks the range displayed in (b) and (e), respectively. L1–L4 denote four different layers growing at the given time.

parameters were set to be the same as in the experiment. The simulated SXRD peaks in Fig. 4(a) are very similar to those in Ref. [14]. Figure 4(b) shows a detail of the transient coverage after a selected pulse. The fast increase at the beginning corresponds to the rapid condensation of new units in the layer, while the transient part is a result of the interlayer transport from the higher level. The transient part is fitted by the biexponential curve, with parameters taken from Ref. [14]. It can be seen that even though the overlap is not perfect, the points are very close to the line. We note that an analogous biexponential behavior observed in a somewhat different case of molecular beam epitaxy growth has been explained in a similar way [29].

The morphology can be significantly altered by introducing the ES barrier and lowering the surface binding energy correspondingly, as shown in Figs. 4(c) and 4(f). The increased ES barrier causes the resulting islands to be more compact, while the SXRD shape [Fig. 4(d)] is similar to the one in Fig. 4(a). The interlayer transport [Fig. 4(e)] can still be successfully fit using the same time constants as in Fig. 4(b) and in Ref. [14].

The similarity of the results obtained by our model and from experiments suggests that the biexponential behavior of the changes of the coverages can be simulated considering the basic processes, dissolution, and interlayer transport. The model, even though strongly simplified, describes well the biexponential character of the interlayer transport, without need of separation to fast and slow transports. One scale is given by the dissolution and jump down of units with no neighbors and the other is given by dissolution and jump down of units with one neighbor.

V. DISCUSSION

In the previous section, we applied our model on the LBL growth by PLD. We proceed by discussing the model limitations arising due to the implemented simplifications.

First, the model neglects the inner chemical structure of the growing material and all partial chemical processes, assuming the final unit is much more stable than the intermediates. In some cases, the intermediates may influence the kinetics and the model could not be used. For example, if two chemical or crystal structures are competing during the growth, the model would necessarily fail.

The model in the present form also cannot be applied when binding energies vary from layer to layer, typically due to relaxation of the lattice during a strained growth. It can be adapted to the growth in which the relaxation can be approximated by level-dependent binding energies without the need to change the layer geometries. Such modification would not significantly increase the computational time.

Another application for which the model cannot be used is the diffusion-controlled growth, in which case the diffusion speed cannot be approximated as infinitely fast. For example,

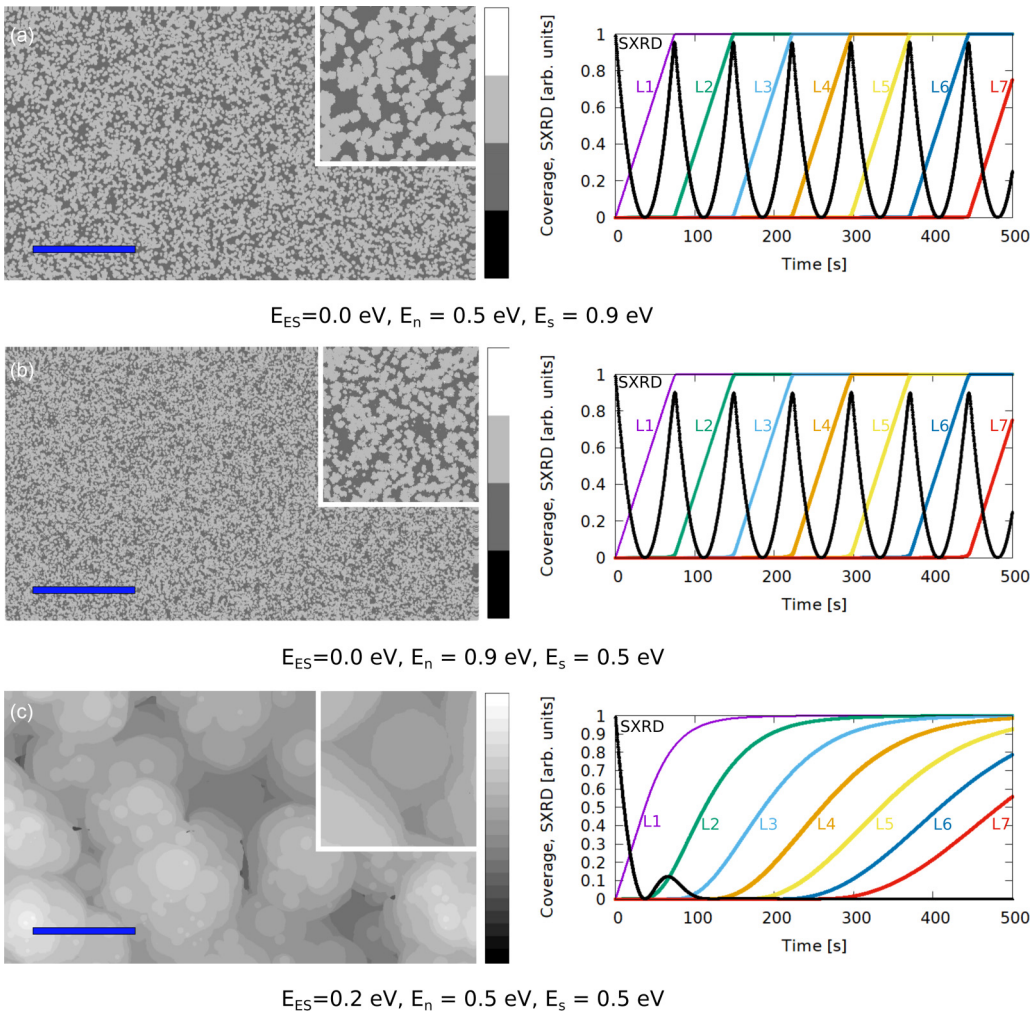

FIG. 5. Morphologies and SXRDs for various binding energies and Ehrlich-Schwoebel barriers: the L1–L9 labels denote the layer, the blue line is 0.5 μm long, and the size of one molecule is considered to be 0.533 nm. The size of the insets is 500 × 500 units, i.e., 266.5 × 266.5 nm.

the model does not realistically describe situations in which some kinetically blocked sites cannot be reached by diffusion.

Finally, we discuss the consequences of 2D gas density ρ_i common for whole level i. As an example, we use the morphology in Fig. 5(c), where the growth is close to 3D island growth. Note that levels i of islands separated by deep trenches share the same units of the gas. However, this is not an issue for the simulation of the growth, if it is not diffusion controlled, as discussed above. In a realistic case with a large ES barrier, the probability of impingement and condensation of a unit on a selected island A is proportional to its uncovered area S_A. In the presented model, the unit impinges to whole level i with the probability proportional to θ_i, but its condensation on island A is proportional to S_A/θ_i, thus giving the same results as in the realistic case.

In this paper, we used the results of the kMC simulations for the calculation of the SXRD intensity I_X in an anti-Bragg point using Eq. (2). This intensity depends only on the monolayer coverages θ_n and is not affected at all by the surface morphology. In order to asses the island sizes and shapes, diffuse x-ray scattering is used, which measures the distribution $I_X(\boldsymbol{Q})$ of scattered x-ray intensity in point $\boldsymbol{Q}$ of reciprocal space close to a chosen reciprocal lattice point [30]. The kMC method presented here is quite suitable for this kind of simulation since the simulation area is larger than the coherence width of a typical x-ray experiment so that the calculating function $I_X(\boldsymbol{Q})$ is nearly averaged over a statistical ensemble of all surface configurations. These simulations, along with a comparison with experimental data, will be the subject of a forthcoming paper.

VI. CONCLUSION

We have presented the kinetic Monte Carlo model which can be very well used to simulate the LBL growth of homogeneous thin films. By using a 2D gas of units as a source of condensing particles, we reached linear scaling of the computational time with the size of the substrate. This scaling allows simulations of large substrates and long deposition times without the need to use nonphysical deposition rates. We have demonstrated that the model is well suited for simulations of PLD growth far from thermodynamic equilibrium.

The model has been applied to the problem of interlayer transport during STO growth by PLD [14]. Our model fits well

the experimental data by simulating the interlayer transport driven by the dissolution of differently bound units and their subsequent jump to a lower layer. The fast and slow transports reflect the dissolution of units without and with one condensed neighbor, respectively.

The model can be used as a base for large-scale simulations of layered growth via fast diffusing units in the case of a wide range of materials, if intermediate chemical reactions can be neglected. The micrometer domain size, not achievable by the standard kMC technique, will allow simulations of *in situ* x-ray scattering, highly sensitive to the morphology of the growing layer.

ACKNOWLEDGMENTS

This work was supported by the Czech Science Foundation (Project No. 19-10799J) and the Charles University Grant Agency (Project No. 660218).

APPENDIX: INFLUENCE OF INTERACTION ENERGIES AND THE EHRLICH-SCHWOEBEL BARRIER

Here we demonstrate the physically relevant behavior of the model by varying the binding energies and the ES barrier. The comparison also shows the wide range of different kinds of growth modes for which the model can be used. As a reference, we use the growth simulation shown in Fig. 3(a).

Figure 5 shows morphologies, SXRDs, and coverages of discrete layers obtained by varying important parameters of the model—the binding energies and the ES barrier. In all cases, the repetition and deposition rates were 5 Hz and 0.0135 ML/s.

The results of the simulation with the surface binding energy E_s increased to 0.9 eV are presented in Fig. 5(a). The morphology shows that the size of the islands is smaller than in the reference case. This is caused by the fact that the probability of cluster dissolution is lower when the binding energy is increased. The rate at which the small clusters dissolve is smaller, thus allowing the nuclei to live long enough to form larger stable islands. From the enlarged part, it is also observable that the shape is not as faceted as in the reference case because of the higher stability of the low-coordinated units. The maxima in SXRD plots are not as high as in the reference case, which means that each layer starts growing before the previous one is fully closed. This is, again, caused by the lower dissolution rate of the small clusters.

Figure 5(b) contains results for the neighbor binding energy E_n increased to 0.9 eV. The islands are even smaller than in both previous cases. From the detail of the morphology, it is obvious that the islands can no longer be considered faceted, but with a rather ragged shape. This is caused, again, by the decreased dissolution rate. The effect is stronger than in the previous cases because, in the calculation of the activation energy [Eq. (1)], the neighbor binding energy is multiplied by the number of neighbors. As a result, any condensed unit with three or more neighbors is stable in the timescales of the simulation. A close inspection of the detail of the morphology shows that there are some condensed units on the higher level—tiny bright dots. Since the picture is taken right before a deposition pulse, the dots indicate that a new level starts growing before the currently active one is fully closed. This claim is also supported by the corresponding SXRD and level coverages. The maxima of the SXRD are lower and the lines showing the coverages of each level are slightly bent near zero and unity.

The effect of the nonzero ES barrier is shown in Fig. 5(c). The difference is immediately obvious. Because of the limited flux of material to the lower level, the growth is no longer 2D island growth, but instead 3D islands are formed. Since both binding energies E_s and E_n are small, the edges of the islands are again smooth and faceted, as in the reference case [Fig. 3(a)], and there are no small unstable clusters present. From the SXRD, it is observed that the growth is LBL only at the beginning. After that the layers are not fully closed before a new layer starts growing. This causes the coverages to not grow as fast as in the other cases.

The growth of 3D islands can be achieved only with a nonzero ES barrier or with another mechanism effectively decreasing the material transport to lower levels. If the binding energies are set high to slow down the dissolution, a hit-and-stick growth is obtained. In order to get more compact islands, the binding energies must be decreased, which results in 2D growth if the ES barrier is not active.

[1] D. G. Schlom, L.-Q. Chen, X. Pan, A. Schmehl, and M. A. Zurbuchen, J. Am. Ceram. Soc. **91**, 2429 (2008).
[2] H. Tanaka, Epitaxial growth of oxide films and nanostructures, in *Handbook of Crystal Growth*, 2nd ed., edited by T. F. Kuech (North-Holland, Boston, 2015), pp. 555–604.
[3] H. Fujioka, Pulsed laser deposition (PLD), in *Handbook of Crystal Growth*, 2nd ed., edited by T. F. Kuech (North-Holland, Boston, 2015), pp. 365–397.
[4] G. Rosenfeld, B. Poelsema, and G. Comsa, Epitaxial growth modes far from equilibrium, in *Growth and Properties of Ultrathin Epitaxial Layers*, edited by D. A. King and D. P. Woodruff (Elsevier Science, Amsterdam, The Netherlands, 1997), pp. 66–101.
[5] Y. Maeno, H. Hashimoto, K. Yoshida, S. Nishizaki, T. Fujita, J. G. Bednorz, and F. Lichtenberg, Nature (London) **372**, 532 (1994).
[6] J. Robertson, C. W. Chen, W. L. Warren, and C. D. Gutleben, Appl. Phys. Lett. **69**, 1704 (1996).
[7] A. R. Akbashev, A. S. Semisalova, N. S. Perov, and A. R. Kaul, Appl. Phys. Lett. **99**, 122502 (2011).
[8] J. Shen, Z. Gai, and J. Kirschner, Surf. Sci. Rep. **52**, 163 (2004).
[9] S. Gerhold, M. Riva, B. Yildiz, M. Schmid, and U. Diebold, Surf. Sci. **651**, 76 (2016).
[10] W. Zhaoyang, S. Liyuan, and H. Lizhong, Vacuum **85**, 397 (2010).
[11] J. A. Venables, Philos. Mag. **27**, 697 (1973).
[12] J. A. Venables, G. D. T. Spiller, and M. Hanbucken, Rep. Prog. Phys. **47**, 399 (1984).
[13] A. C. Barato, H. Hinrichsen, and D. E. Wolf, Phys. Rev. E **77**, 041607 (2008).
[14] G. Eres, J. Z. Tischler, C. M. Rouleau, P. Zschack, H. M. Christen, and B. C. Larson, Phys. Rev. B **84**, 195467 (2011).

[15] S. Chen, B. Merriman, M. Kang, R. E. Caflisch, C. Ratsch, L.-T. Cheng, M. Gyure, R. P. Fedkiw, C. Anderson, and S. Osher, J. Comput. Phys. **167**, 475 (2001).
[16] R. E. Caflisch, J. Sci. Comput. **37**, 3 (2008).
[17] L. Huang, Micro Nano Lett. **13**, 1497 (2018).
[18] Z. Zhu, X. J. Zheng, and W. Li, Appl. Surf. Sci. **256**, 5876 (2010).
[19] R.-Q. Zhang, X.-H. Xu, S.-Y. Zhang, and G. A. Gehring, Phys. Rev. B **78**, 075419 (2008).
[20] M. R. Rashidian Vaziri, F. Hajiesmaeilbaigi, and M. H. Maleki, J. Appl. Phys. **110**, 043304 (2011).
[21] T. Weckman, M. Shirazi, S. D. Elliott, and K. Laasonen, J. Phys. Chem. C **122**, 27044 (2018).
[22] G. Ehrlich and F. G. Hudda, J. Chem. Phys. **44**, 1039 (1966).
[23] R. L. Schwoebel and E. J. Shipsey, J. Appl. Phys. **37**, 3682 (1966).
[24] A. Bortz, M. Kalos, and J. Lebowitz, J. Comput. Phys. **17**, 10 (1975).
[25] P. A. Maksym, Semicond. Sci. Technol. **3**, 594 (1988).
[26] I. K. Robinson and D. J. Tweet, Rep. Prog. Phys. **55**, 599 (1992).
[27] G. Eres, J. Tischler, C. Rouleau, B. Larson, H. Christen, and P. Zschack, Real-time studies of epitaxial film growth using surface X-ray diffraction (SXRD), in *In Situ Characterization of Thin Film Growth*, Woodhead Publishing Series in Electronic and Optical Materials, edited by G. Koster and G. Rijnders (Woodhead, Cambridge, UK, 2011), pp. 239–273.
[28] A. Ichimiya and P. I. Cohen, *Reflection High-Energy Electron Diffraction* (Cambridge University Press, Cambridge, 2004).
[29] D. D. Vvedensky and S. Clarke, Surf. Sci. **225**, 373 (1990).
[30] U. Pietsch V. Holý and T. Baumbach, *High-Resolution X-Ray Scattering* (Springer, New York, 2004).